

Hydrostatic Pressure Induced Anomalous Enhancement in the Thermoelectric Performance of Monolayer MoS₂

Saumen Chaudhuri,¹ Amrita Bhattacharya,² A. K. Das,¹ G. P. Das,³ and B. N. Dev^{4,5,*}

¹*Department of Physics, Indian Institute of Technology Kharagpur, Kharagpur 721302, India*

²*Department of Metallurgical Engineering and Materials Science,
Indian Institute of Technology Bombay, Mumbai 400076, India*

³*Research Institute for Sustainable Energy, TCG Centres for Research and
Education in Science and Technology, Sector V, Salt Lake, Kolkata 700091, India*

⁴*Department of Physics and School of Nano Science and Technology,
Indian Institute of Technology Kharagpur, Kharagpur, 721302, India*

⁵*Centre for Quantum Engineering, Research and Education,*

TCG Centres for Research and Education in Science and Technology, Sector V, Salt Lake, Kolkata 700091, India

(Dated: August 2, 2023)

The hydrostatic pressure induced changes in the transport properties of monolayer (ML) MoS₂ have been investigated using first-principles density functional theory based calculations. The application of pressure induces shift in the conduction band minimum (CBM) from K to Λ , while retaining the band extrema at K in around the same energy at a pressure of 10 GPa. This increase in valley degeneracy is found to have a significant impact on the electronic transport properties of ML-MoS₂ via enhancement of the thermopower (S) by up to 140% and power factor ($S^2\sigma/\tau$) by up to 310% at 300 K. Besides, the very low deformation potential (E_{DP}) associated with the CB- Λ valley results in a remarkably high electronic mobility (μ) and relaxation time (τ). Additionally, the application of pressure reduces the room temperature lattice thermal conductivity (κ_L) by 20% of its unstrained value, owing to the increased anharmonicity and resulting increase in the intrinsic phonon scattering rates. The hydrostatic pressure induced increase in power factor ($S^2\sigma$) and the decrease in κ_L act in unison to result in a substantial improvement in the overall thermoelectric performance (zT) of ML-MoS₂. At 900 K with an external pressure of 25 GPa, zT values of 1.63 and 1.21 are obtained for electron and hole doping, respectively, which are significantly higher compared to the zT values at zero pressure. For the implementation in a thermoelectric module where both n-type and p-type legs should be preferably made of the same material, the concomitant increase in zT of ML-MoS₂ for both types of doping with hydrostatic pressure can be highly beneficial.

Keywords: DFT, hydrostatic pressure, MoS₂, thermoelectric properties

I. INTRODUCTION

The search for renewable energy sources has become a quintessential challenge for mankind [1]. Thermoelectric materials (TEMs), which can convert a difference in temperature into useful voltage based on the principle of Seebeck effect [2, 3], may aid to it via waste heat recovery [4]. The efficiency of a thermoelectric material depends on a dimensionless parameter called the thermoelectric figure of merit (zT), which is expressed as $zT = \frac{S^2\sigma}{\kappa}T$. zT is directly proportional to the product of square of Seebeck coefficient S and the electrical conductivity σ , while is inversely proportional to the total thermal conductivity, $\kappa = \kappa_e + \kappa_L$, which is the sum of the electrical (κ_e) and the lattice thermal conductivity (κ_L), at a given temperature T . Tuning the zT of a given TEM is an extremely tedious task, since the transport parameters i.e. the S , σ , and κ_e are inter-dependent on each other, as they all depend on the electronic carrier concentration (n). Therefore, the two main routes that can be followed to maximize the zT are (a) engineering the electronic band structure to optimize the power factor [5, 6] and (b) phonon engineering for lowering the κ_L of the material [7–11].

More recently, the two dimensional planar materials have garnered a lot of interest in thermoelectric research owing to their unique properties arising from quantum confinement effects. The excellent combination of electrical and thermal transport in these 2D materials leads to a significantly large thermoelectric zT [5, 7]. Over the years, various 2D materials, viz. transition metal dichalcogenides (TMDCs) (e.g., MoS₂, WS₂, MoSe₂, and HfS₂), group IVA-VA compounds (e.g., SnSe, SnS, GeSe) etc., have emerged as potential TEM with reasonably good thermoelectric performance [12–15]. In recent times, especially the layered TMDCs have drawn significant interest owing to their tunable band gap, high electrical mobility and low thermal conductivity [16–20]. Some of the TMDCs, such as WS₂

* corresponding author: bhupen.dev@gmail.com

[21], WSe₂ [22], HfS₂ [23], SnSe₂ [24] etc., have shown notably high thermoelectric efficiency. Among the family of TMDCs, MoS₂ has been explored extensively as a potential thermoelectric material, both theoretically [19, 25–31] and experimentally [32, 33], and the monolayer (ML) counterpart appears to be a reasonably good thermoelectric material [25, 28, 30, 32, 33]. Kedar *et al* [32] have measured the room temperature thermoelectric power factor of ML-MoS₂ to be 8.5 mWK⁻²m⁻¹, which is comparable to the well known thermoelectric materials, such as Bi₂Te₃. Buscema *et al* [34] have found a large Seebeck coefficient in ML-MoS₂, which is also tunable by an external electric field. However, the zT value obtained with ML-MoS₂ is very low (i.e., a zT value of only ~ 0.11 is achieved with ML-MoS₂ at 500 K [13]), which is not useful for practical purposes. The primary reason behind the low thermoelectric efficiency of ML-MoS₂ is derived from its rather high lattice thermal conductivity (κ_L), which is considerably higher compared to the other analogous TMDCs, such as WSe₂, ZrS₂, HfS₂ etc. [12, 21, 35–37]. Therefore, finding out a way by which both the power factor ($S^2\sigma$) and the κ_L can be optimized simultaneously in a way to maximize the thermoelectric zT of ML-MoS₂ has been an extensive quest.

Efforts have been made to improve the thermoelectric efficiency of ML-MoS₂ by applying an external electric field [34] or mechanical strain [11, 23, 25, 28, 30, 31]. Doping with impurity atoms and hybridization are the widely explored avenues in improving the zT of a material [9, 38, 39]. In-plane strain engineering has also been employed routinely to tune the electronic and thermoelectric properties of various 2D materials, such as WS₂, ZrS₂, HfS₂, ZnO etc. [12, 23, 40, 41]. In one of our earlier studies, we have seen that in-plane tensile strains, in general, and strains along the zig-zag direction, in particular, can significantly enhance the thermoelectric efficiency of ML-MoS₂ [31]. However, the implementation of different in-plane strains in experiments is a daunting task [42–46]. Application of hydrostatic pressure, on the other hand, can be a potential alternative easier route that can be achieved experimentally owing to the fairly simple procedure and reversibility. Previous theoretical and experimental studies on the pressure dependence of electronic properties, structural parameters and elastic constants of bulk MoS₂ suggest that hydrostatic pressure might be effective in tuning its transport properties [29, 47–49]. Zhang *et al* demonstrated that the thermoelectric performance of bulk MoS₂ can be enhanced by the application of hydrostatic pressure [29]. For ML-MoS₂, the variation in the thermoelectric parameters with various in-plane strain has been studied thoroughly over the years [11, 23, 25, 28, 30, 31]. However, studies on the effect of hydrostatic pressure on the transport properties of ML-MoS₂ are lacking.

Interestingly, in a recent study, a direct K-K to indirect K- Λ band gap transition has been optically detected in ML-MoS₂ under hydrostatic pressure [48]. Therefore, a pressure induced shift of the conduction band minimum (CBM) from K to Λ is inevitable. At the critical pressure, exploiting the degeneracy of the conduction band edges at K and Λ , an enhancement in the thermoelectric performance of ML-MoS₂ can be achieved. Also, the overall transport mechanism, both electronic and lattice, in ML-MoS₂, can be tuned continuously and controllably by the application of pressure. The hydrostatic pressure induced modification in the transport properties of ML-MoS₂ has not been studied theoretically or experimentally. Therefore, a thorough investigation of the underlying mechanism is necessary. This may pave the way for the application of ML-MoS₂ or any other semiconducting TMDCs in future commercial thermoelectric devices. In the present work, we have undertaken a theoretical investigation of hydrostatic pressure-mediated modification in the thermoelectric properties of ML-MoS₂.

II. COMPUTATIONAL DETAILS

First-principles calculations have been performed under the framework of ab-initio density functional theory (DFT) as implemented in the Vienna Ab Initio Simulation Package (VASP) [50, 51] with projector augmented wave (PAW) potentials to account for the electron-ion interactions [52]. The electronic exchange and correlation (XC) interactions are addressed within the generalized gradient approximation (GGA) of Perdew-Burke-Ernzerhof (PBE) [53]. In all calculations, the Brillouin zone (BZ) is sampled using a well-converged Monkhorst-Pack [54] k-point set ($21 \times 21 \times 1$), and a conjugate gradient scheme is employed to optimize the geometries until the forces on each atom are found to be less than 0.01 eV/Å. A vacuum thickness of approximately 20 Å has been used to avoid the spurious interaction between the periodic images of the layers. In order to generate the structure under hydrostatic pressure, the bulk lattice of MoS₂ is subjected to external stress of equivalent amount. The electronically optimized strained structure of bulk MoS₂ is then used to cleave one single layer of the MoS₂ from its bulk lattice under different hydrostatic pressures i.e. for 5, 10 and 25 GPa. A similar approach has also been adopted to generate hydrostatic strained structures in earlier reports [48, 55].

The temperature- and carrier concentration-dependent changes in the thermoelectric parameters such as the Seebeck coefficient (S), electrical conductivity (σ), power factor ($S^2\sigma$) etc. have been calculated by using the energy eigen values to solve the semi-classical Boltzmann transport equation as implemented within the BoltzTraP code [56]. All the transport properties have been calculated within the constant relaxation time approximation (CRTA) which assumes that the charge carrier relaxation time does not vary with energy or carrier concentration. To go beyond the

CRTA, the charge carrier mobility (μ) and relaxation time (τ) are explicitly determined using the acoustic deformation potential (ADP) theory developed by Bardeen and Shockley [57]. Considering the scattering between charge carriers and longitudinal acoustic phonons, the μ and τ of the 2D materials are computed as $\mu = \frac{2e\hbar^3 C_{2D}}{3k_B T m^{*2} (E_{DP})^2}$ and $\mu = \frac{e\tau}{m^*}$, where C_{2D} is the effective elastic constant, m^* is the carrier effective mass, and E_{DP} is the deformation potential constant corresponding to the conduction and the valence band edges. The material-specific inputs such as the C_{2D} , m^* , and the E_{DP} are determined from first-principles calculations using VASP.

The phonon dispersion curves are calculated based on the supercell approach using the finite displacement method restricting the atomic vibrations to an amplitude of 0.015 Å as implemented in the phonopy code [58]. To compute the lattice transport properties, the Boltzmann Transport Equation (BTE) for phonons is solved under the relaxation time approximation (RTA) as implemented in the phono3py code [59]. The second- and third-order interatomic force constants (IFC) are calculated using convergence-checked $4 \times 4 \times 1$ and $2 \times 2 \times 1$ supercells based on the relaxed unit cell, respectively. Fourth- and higher-order IFCs are not taken into consideration due to their presumably small contribution to lattice thermal transport. Forces are optimized using a fine energy convergence criterion of 10^{-8} eV. Well-converged k-meshes are used to optimize the structures. Supercell method is used to ensure convergence, whereby convergence is reached for $4 \times 4 \times 1$ supercell. To accurately compute the lattice thermal conductivity, a dense q-mesh of $51 \times 51 \times 1$ is used to sample the reciprocal space of the primitive cells. The mode-resolved phonon transport parameters, such as the phonon group velocity (v_λ) and relaxation time (τ_λ) are extracted using python-based extensions.

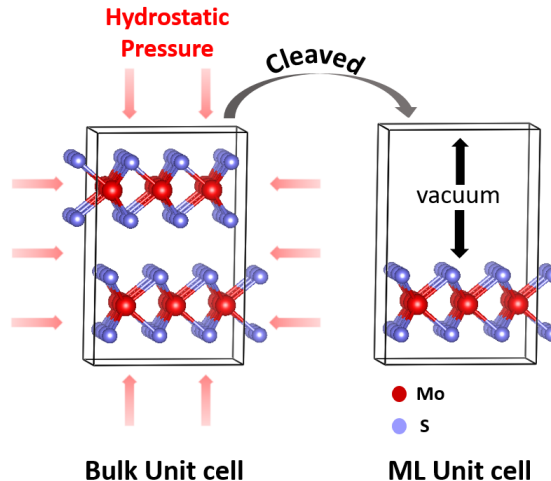


FIG. 1. Schematic diagram illustrating the procedure of obtaining a hydrostatic strained MoS₂ monolayer by cleaving its equivalent strained bulk MoS₂ counterpart.

III. RESULTS AND DISCUSSION

A. Structure parameters and electronic properties

The single-layer counterpart of MoS₂ forms a hexagonal honeycomb crystal structure with the Mo and S atoms arranged in a trigonal prismatic coordination, as can be seen from Fig. 1. A monolayer (ML) structure of MoS₂ consists of one Mo and two S atomic planes arranged in a “sandwich” (S-Mo-S) type structure. The primitive unit cell of bulk MoS₂ comprises of two such monolayers with an inter-layer separation (t) of 6.15 Å. The structural parameters of both the bulk- and the ML-MoS₂, calculated herein, are in good agreement with earlier reports [28, 31]. To study the effect of hydrostatic pressure on the electronic and transport properties of ML-MoS₂, different pressures of up to 25 GPa have been applied. A schematic of the pressure application on ML-MoS₂ is presented in Fig. 1. To confirm the dynamic stability of the crystal structure, phonon dispersion has been calculated at each pressure. From the electronic structure calculations, ML-MoS₂ in its pristine form is found to be a direct band gap semiconductor with both the valence band maximum (VBM) and the conduction band minimum (CBM) located at the same high-symmetry point i.e. at the K (0.33, 0.33, 0) point of the Brillouin zone (BZ). The band gap value of pristine ML-MoS₂ is found to be 1.68 eV, which is in agreement with previous theoretical works [19, 28, 60].

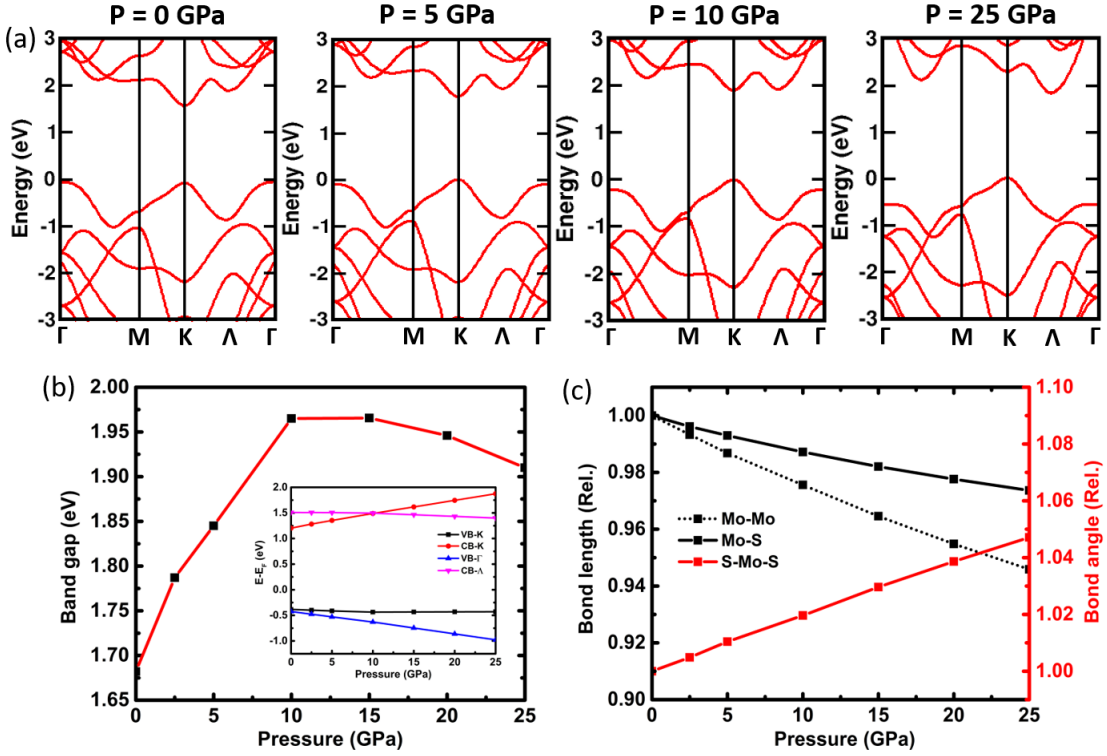


FIG. 2. (a) Band dispersion along the high symmetry path of ML-MoS₂ at different values viz. 0 GPa, 5 GPa, 10 GPa, and 25 GPa of hydrostatic pressure. The pressure values are given at the top of the corresponding band structure plots. (b) The variation in the band gap as a function of the hydrostatic pressure (b: inset shows the energies corresponding to the valence and conduction band edges at different k-points with reference to the Fermi energy E_F). (c) The various structural parameters i.e. the bond length (shown in black) and bond angle (shown in red) of ML-MoS₂ as a function of hydrostatic pressure.

The hydrostatic pressure induced effects on the structural parameters and electronic structure of ML-MoS₂ are presented in Fig. 2. From the band structure plots it can be seen that, with the application of pressure, the CBM at K point (CB-K) shifts toward higher energy (i.e. away from the Fermi level), while the energy shift in the valence band top at K (VB-K) is nominal. Therefore, the band gap increases initially, until $P = 10$ GPa, as can be seen from the variation in the band gap with pressure shown in Fig. 2 (b). At a pressure around 10 GPa, the CBM shifts to the Λ -point i.e., midway along the K- Γ path, while the one extrema at the K point lying very close in energy, thereby forming degenerate energy valleys in the conduction band. Such valley or band degeneracies are found to have useful implications in enhancing the thermoelectric performance of a material [5, 6]. Starting from 15 GPa, when the CBM is at the Λ point, the band gap starts to decrease with increasing pressure. To quantify the energy shifts, the energies corresponding to the VB and the CB edges are plotted as a function of pressure and presented in Fig. 2 (b). It is clear that the energy shifts in the CB-K and the VB- Γ are significantly higher compared to the energy shifts in other valence and conduction band extrema.

To understand these energy shifts in greater detail, we have calculated the band decomposed charge densities corresponding to the relevant valence and conduction band edges, such as the CB at K (CB-K), CB at Λ (CB- Λ), VB at K (VB-K) and VB at Γ (VB- Γ) (see Fig. S1 in supplementary material). The band edges at different k-points in the BZ are found to have very different real space charge densities, however, mostly comprising of the Mo- d orbital. For example, the states at CB-K and VB-K are predominantly comprising of Mo- d character arising from d_{z^2} and $d_{x^2-y^2}$ orbitals, respectively. The states at CB- Λ and VB- Γ , on the other hand, have a certain admixture of S- p orbitals along with the Mo- d orbitals. With the application of pressure, both the Mo-Mo and Mo-S bond length decreases with an increase in the S-Mo-S bond angle and therefore, the S-S interplanar distance, as can be seen from Fig. 2 (c). However, the magnitude of reduction in Mo-Mo bond length is much higher compared to that of Mo-S bond length. It is, therefore, expected that the states that are composed purely of Mo- d orbitals (such as CB-K), and thus depend entirely on the Mo-Mo bond length, will experience larger energy shifts compared to the states that comprise of both Mo- d and S- p character (such as CB- Λ). The large energy shifts of the CB-K, which is the most relevant one in this case, can be understood by analysing the pressure induced modifications in the structural parameters. With increasing bond angle and decreasing bond length under pressure, the interaction strength between the Mo- $d_{x^2-y^2}$

and S-*p* orbitals weakens, while the coupling between the d_{z^2} orbitals will strengthen. Therefore, the energy splitting of the pair of states with predominantly Mo- d_{z^2} character, such as at CB-K and VB- Γ , increases under pressure and thereby, shifting the CB-K towards the higher energy.

B. Thermoelectric transport properties

To understand the implications of the pressure induced modifications in the electronic band structure of ML-MoS₂, various thermoelectric transport parameters, such as the Seebeck coefficient or thermopower (S), electrical conductivity (σ), power factor (PF: $S^2\sigma$) and the charge carrier mobility (μ) have been investigated as a function of increasing hydrostatic pressure. Specifically, the pressure induced degeneracy in the conduction band is expected to have a significant impact on the thermoelectric parameters of ML-MoS₂. The pressure induced variation in the S and PF as a function of carrier concentration at a fixed temperature $T = 300$ K, and as a function of temperature at a fixed carrier concentration of $N_{2D} = 1.3 \times 10^{13}$ /cm² are presented in Fig. 3 for both the n-type (shown in top panel) and p-type (shown in the bottom panel) doping. With increasing pressure, the S is found to increase significantly for n-type doping concentration of $0.01 - 3 \times 10^{13}$ /cm². The highest value of S can be achieved at a hydrostatic pressure of 10 GPa, which is due to the pressure induced valley degeneracy at CB-K and CB- Λ . At this pressure owing to the increased valley degeneracy at the CB edge, the density of states effective mass (m_d^*) increases, thereby resulting in an enhancement of the S , without explicitly affecting the charge carrier mobility (μ). Therefore, the power factor is significantly improved due to the degenerate valleys. However, with pressure the valley degeneracy at the valence band extrema is lost, since the band maximum at the Γ point shifts to lower energy and the band maximum is found to lie only at the K-point. Due to this loss in valley degeneracy in the valence band, a reduction in S is incurred upon hole doping. For both electron and hole doping, the thermopower decreases with increasing carrier concentration, which is a typical characteristic of any semiconducting material. Owing to the increase in S , a significant enhancement in the relaxation time (τ) scaled power factor ($S^2\sigma/\tau$) is observed as well under the application of hydrostatic pressure for electron doping (see Fig. 3 (a) and (b)). The power factor value reaches up to 8.5×10^{10} W/mK²s at 300 K for electron doping at a pressure of 10 GPa, which is significantly higher compared to the zero pressure power factor values. The power factor represents the ability of a material to produce useful electrical power at a given temperature gradient. Therefore, the large power factor is indicative of better thermoelectric performance. Also, the Goldsmid-Sharp relation [61] is found to hold well, as the variation in the maximum achievable thermopower (S_{\max}) with applied pressure at a fixed temperature follows the same trend as that of the band gap (see Fig. S2 in supplementary material). The relation is given as, $E_g = 2eS_{\max}T$, where E_g is the band gap, and S_{\max} is the maximum attainable thermopower at any temperature T . It is, therefore, clear that both the electronic and the thermoelectric parameters are equally sensitive to the applied pressure.

In order to understand the temperature dependency, the variation in the thermoelectric parameters of ML-MoS₂ is investigated for temperature in a range of 100 K-900 K at a fixed carrier concentration of 1.3×10^{13} /cm², which corresponds to 5×10^{19} /cm³ in bulk configuration. The upper limit of the temperature is well within the thermal stability regime of ML-MoS₂, which was analyzed using molecular dynamics (MD) calculations in our earlier work [31]. The S and PF are plotted as function of temperature for different hydrostatic pressure under electron and hole doping (see Fig. 3 (b) and (d)). For the electron doping, both these quantities are found to be highest at a pressure of 10 GPa for the entire temperature range due to the increased degeneracy at the CBM. However, for the hole doping the pristine one is found to show higher S and PF as compared to their pressurized counterparts for the entire temperature range, which is due to the loss of the valley degeneracy at the VBM under pressure (see Fig. 3 (d)). For both electron and hole doping, the PF is found to increase dramatically with increasing temperature. At 900 K, the highest PF values obtained for electron and hole doping are 16×10^{10} W/mK²s and 8×10^{10} W/mK²s, respectively. This is indicative of the possible use of ML-MoS₂ as a high temperature thermoelectric material.

The transport parameters calculated herein, such as the σ , κ_e and PF ($S^2\sigma$) are scaled by the charge carrier relaxation time (τ), since the calculations performed here are based on the constant relaxation time approximation (CRTA). CRTA assumes that the carrier relaxation time (τ) and therefore, the mobility (μ) does not vary strongly with energy. Such an oversimplified assumption often lead to misleading conclusions. In the present case, the explicit determination of τ and μ is essential, since τ and μ itself are functions of external applied pressure. In the calculations of μ and τ , only the scattering of charge carriers with longitudinal acoustic phonons within the acoustic deformation potential (ADP) theory of Bardeen and Shockley [57] is considered (see Table 1 in supplementary material). It is assumed that the scattering with the polar optical phonons will have an inconsequential effect owing to the intrinsically non-polar nature of MoS₂. Other scattering events, such as boundary scattering and impurity scattering are also ignored, since these are strongly dependent on experimental conditions. Considering only a part of the total scattering processes, the calculations performed herein are expected to provide only an intrinsic limit of μ and τ , which can be largely overestimated compared to the experimental values.

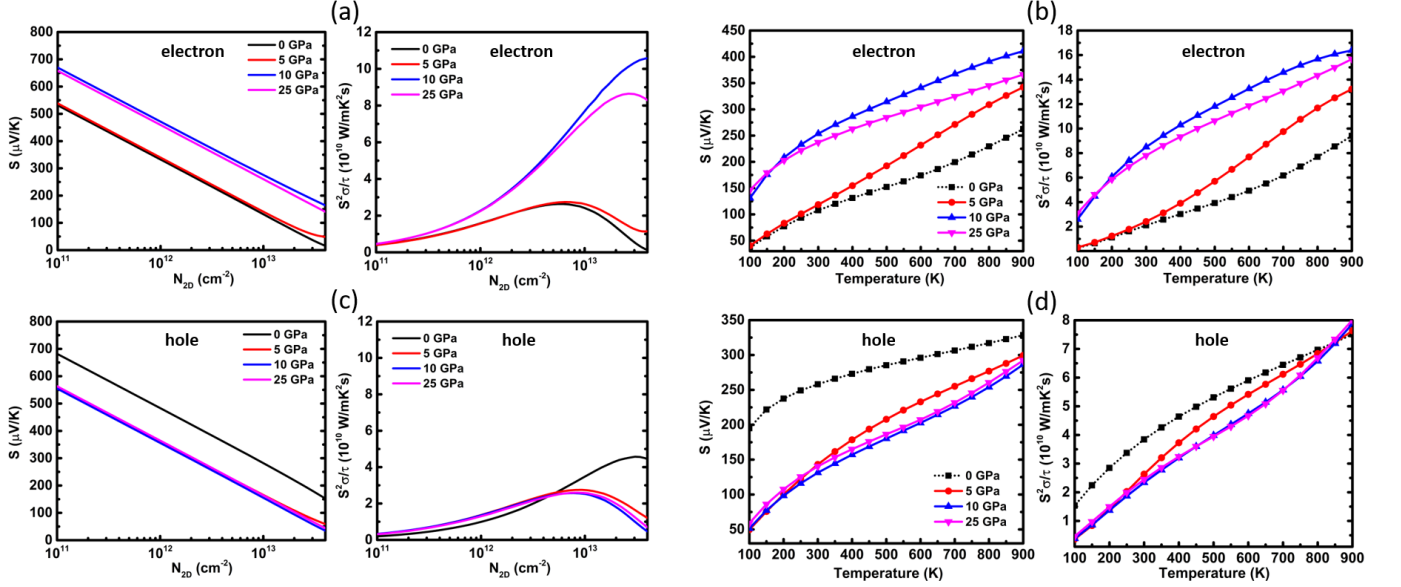


FIG. 3. Variation in the thermoelectric parameters i.e., the thermopower (S) and relaxation time (τ) scaled power factor ($S^2\sigma/\tau$) of ML-MoS₂ for different values of applied hydrostatic pressure as a function of (a, c) carrier concentration (N_{2D}) at a fixed temperature of 300 K and (b, d) as a function of temperature for a fixed electron (upper panel) and hole (lower panel) doping of $1.3 \times 10^{13} / \text{cm}^2$.

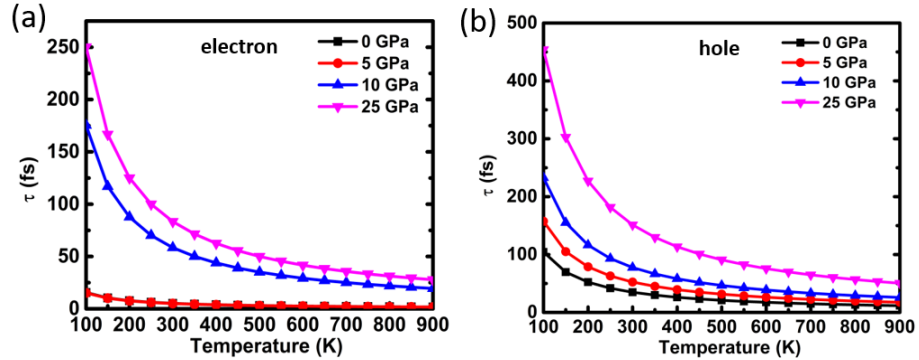


FIG. 4. Variation in the charge carrier relaxation time (τ) of ML-MoS₂ with temperature at different pressure values for (a) electron and (b) hole doping.

The charge carrier relaxation time (τ) of ML-MoS₂ as a function of temperature at different pressure values is shown in Fig. 4, and the carrier mobility (μ) plots are provided in the supplementary material (see supplementary material Fig. S3). The physical parameters that are required for the analytical formulation of the deformation potential theory (DP), such as the elastic constant (C_{2D}), carrier effective mass (m^*) and the deformation potential (E_{DP}) are presented in Table I, and the computed mobility of ML-MoS₂ in the zero pressure case is in good agreement with previous reports [62–64]. Note that, due to the in-plane isotropic nature of ML-MoS₂, the values of the various physical parameters calculated along different directions are found to be identical. Therefore, the simplest form of the Bardeen and Shockley equation, which takes into account the average values of the C_{2D} , m^* , and E_{DP} is implemented in this work. The mobility of electrons and holes at 300 K is found to be 193.6 and 1056.2 $\text{cm}^2\text{V}^{-1}\text{s}^{-1}$, respectively. The relaxation time corresponding to electron and hole scattering decreases with temperature following a parabolic function, as can be seen from Fig. 4 (a) and (b). For both types of carriers, τ increases with increasing pressure. For electrons, τ increases anomalously with pressure, whereas for holes it increases in a monotonic fashion. A sharp increase in μ and τ starting from $P = 10$ GPa is seen for electron doping (see Fig. 4 (a)). As the pressure increases to 10 GPa, the involvement of the conduction band valley at Λ (CB- Λ) in electronic conduction becomes apparent. It can be seen from Table I that, the effective mass of electrons is nearly identical in both the conduction band valleys at K and Λ . However, the deformation potential (E_{DP}) associated with the CB- Λ is more than three times smaller

TABLE I. The calculated effective 2D elastic constant (C_{2D}), the carrier effective mass (m^*), the absolute deformation potential constant (E_{DP}) corresponding to the conduction and valence band edges and the total charge carrier mobility (μ) of ML-MoS₂ at 300 K for different hydrostatic pressures. The m^* and E_{DP} are given for the different band edge positions (K and Λ given in bracket).

P (GPa)	Carriers	C_{2D}	m^* (m_0)	E_{DP} (eV)	μ ($\text{cm}^2\text{V}^{-1}\text{s}^{-1}$)
0	e	212.5	0.47 (K)	6.61 (K)	193.64
	h		0.58 (K)	2.29 (K)	1056.25
5	e	230.0	0.48 (K)	6.88 (K)	186.24
	h		0.58 (K)	1.94 (K)	1597.22
10	e	246.2	0.51 (K), 0.52 (Λ)	6.97 (K), 1.99 (Λ)	1950.69
	h		0.59 (K)	1.63 (K)	2308.22
15	e	295.0	0.52 (Λ)	1.43 (Λ)	2782.38
	h		0.64 (K)	1.22 (K)	4095.06

than that with the CB-K. Therefore, the electronic mobility and relaxation time at the CB- Λ valley is significantly higher compared to that at the CB-K. Thus, the contribution from the CB- Λ results in the remarkable increase in total μ and τ . For holes, on the other hand, the effective mass increases slightly. With increasing pressure, however, due to the large reduction in E_{DP} corresponding to the VBM at K, the hole mobility and therefore, the relaxation time increases. The enhancement in the mobility (μ) and relaxation time (τ) for both electrons and holes is highly beneficial for better thermoelectric performance. The estimated τ values are incorporated in the calculated electronic transport parameters, such as the σ/τ , κ_e/τ and PF ($S^2\sigma/\tau$) to calculate the figure of merit (zT) as discussed in the subsequent paragraph.

The pressure induced modifications in the structural parameters are expected to have certain implications on the lattice transport properties. Therefore, the effect of pressure on the lattice thermal conductivity (κ_L) of ML-MoS₂ has been calculated and the variation in κ_L with temperature at some representative values of pressure is shown in Fig. 5. For pristine ML-MoS₂, the κ_L at 300K is found to be $24.41 \text{ Wm}^{-1}\text{K}^{-1}$, which agrees well with earlier theoretical [35, 65] and experimental reports [36]. The κ_L of ML-MoS₂ decreases with increasing pressure and reduces to $17.48 \text{ Wm}^{-1}\text{K}^{-1}$ at a pressure of 25 GPa. Owing to the inverse relationship of κ_L with the thermoelectric figure of merit (zT), a reduction in κ_L is immensely advantageous in enhancing the thermoelectric performance. The variation in κ_L with temperature is found to follow the $1/T$ law owing to the increased probability of Umklapp scattering. A reduced value of $5.77 \text{ Wm}^{-1}\text{K}^{-1}$ is obtained at 900 K under an external pressure of 25 GPa. The total thermal conductivity (κ), which is a sum of the electronic (κ_e) and the lattice contribution (κ_L), is found to be largely dominated by the lattice counterpart, at all temperature and pressure. This can be explained as the general behaviour of a semiconductor that majority of the heat is carried by the phonons with negligible contribution stemming from the electrons.

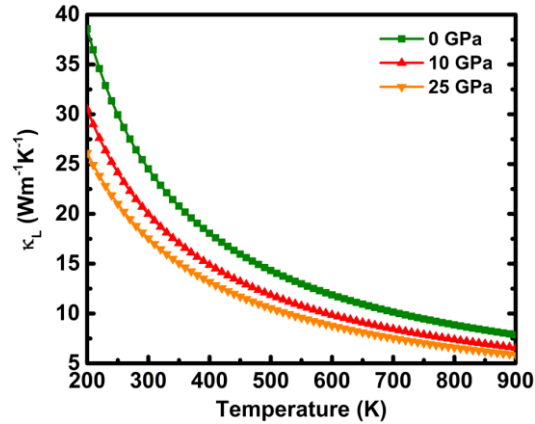


FIG. 5. Variation in the lattice thermal conductivity (κ_L) of ML-MoS₂ with temperature at different values of hydrostatic pressure.

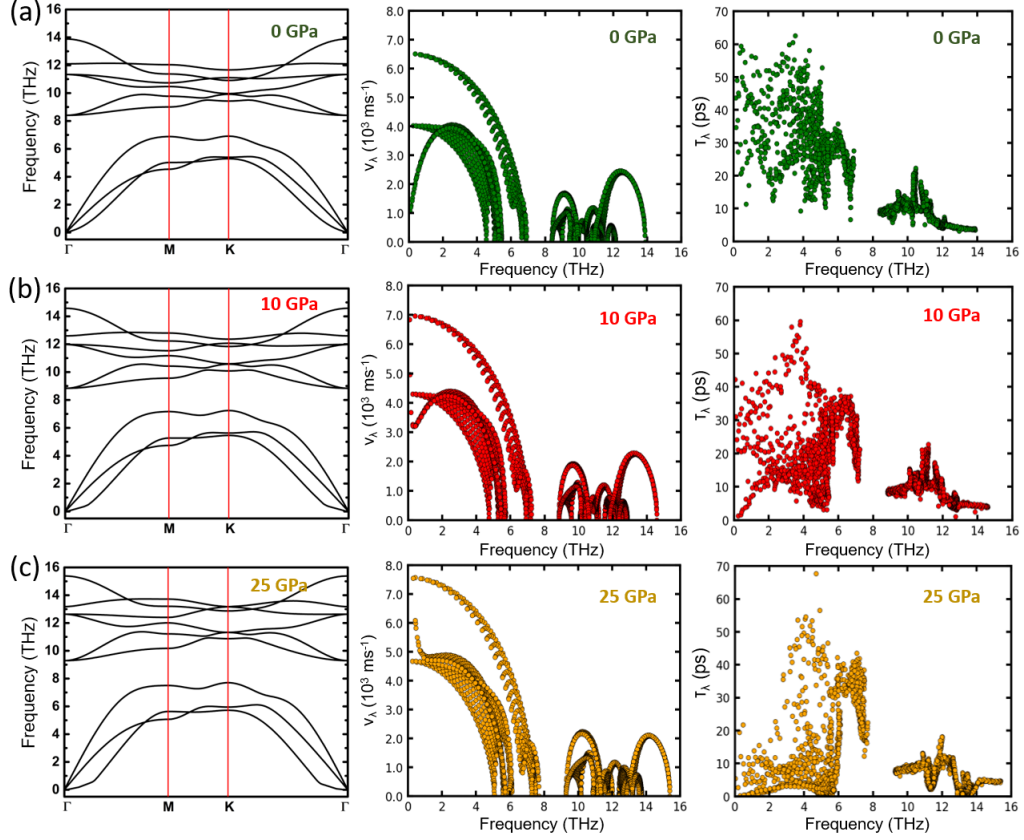


FIG. 6. Phonon band structure (left) along the high-symmetry path Γ -M-K- Γ , (middle) group velocity (v_λ), and (right) scattering time (τ_λ) of ML-MoS₂ at 300 K and at different hydrostatic pressure of (a) 0 GPa, (b) 10 GPa, and (c) 25 GPa.

To investigate the pressure induced reduction in κ_L in greater detail, further analysis of the κ_L is performed. The mode-resolved values of the phonon group velocity (v_λ) and scattering time (τ_λ) for a particular phonon mode λ are computed at 300 K as a function of phonon frequency at different pressures and presented with the corresponding phonon band structures in Fig. 6. It can be seen that, both v_λ and τ_λ of ML-MoS₂ is significantly higher within the frequency range of 0 to 7 THz, which corresponds to the acoustic phonon modes. It is, therefore, clear that the κ_L stemming from the acoustic modes is much higher than the optical modes. With increasing pressure, due to the strengthening of the interatomic bonds, a stiffening of the acoustic phonon modes and a blue shift in the frequency of the optical phonon modes at the zone centre (at Γ) is observed. Thereby, the v_λ associated with the acoustic phonon modes increases slightly. However, the phonon scattering time (τ_λ) reduces significantly with increasing pressure, as can be seen in Fig. 6. Owing to the large decrease in τ_λ , the κ_L decreases with pressure.

In order to understand the pressure induced large reduction in τ_λ , the crystal anharmonicity and three-phonon scattering rate of ML-MoS₂ are computed at 300 K for two representative pressures, 0 GPa and 10 GPa, and shown in Fig. 7. The phonon scattering rate is strongly influenced by the crystal anharmonicity. In fact, it is the anharmonic vibration that limits the κ_L to a finite value. The bond anharmonicity measures the asymmetry in atomic vibration, which can be characterized by the mode Grüneisen parameters (γ_i), defined as $\gamma_i = -\frac{V_0}{\omega_i} \frac{\Delta\omega_i}{\Delta V}$, where ω_i is the frequency of the phonon mode i at the equilibrium volume V_0 . The Grüneisen parameter (γ) of ML-MoS₂ has the highest magnitude in the low frequency regime (0-2 THz), which belongs to the low frequency acoustic modes, albeit mainly the out-of-plane acoustic mode or the ZA mode. With increasing pressure, the mode Grüneisen parameter (γ_i) corresponding to the ZA mode increases, as can be seen from Fig. 7 (a) and (b). Therefore, the anharmonic phonon scattering rates are expected to increase with increasing pressure. Now, the anharmonicity giving rise to the scattering events involving three phonons has two possible scattering channels. One is the absorption process (+), where two phonons combine to produce the third phonon. The other one is the emission process (-), where one phonon splits into two different phonons. The scattering rates corresponding to the two processes, absorption (τ_+^{-1}) and emission (τ_-^{-1}), are plotted as a function of phonon frequency (see Fig. 7), and the total scattering rate ($\tau^{-1} = \tau_+^{-1} + \tau_-^{-1}$) is provided in the supplementary material (see Fig. S4 in supplementary material). Due to the energy conservation

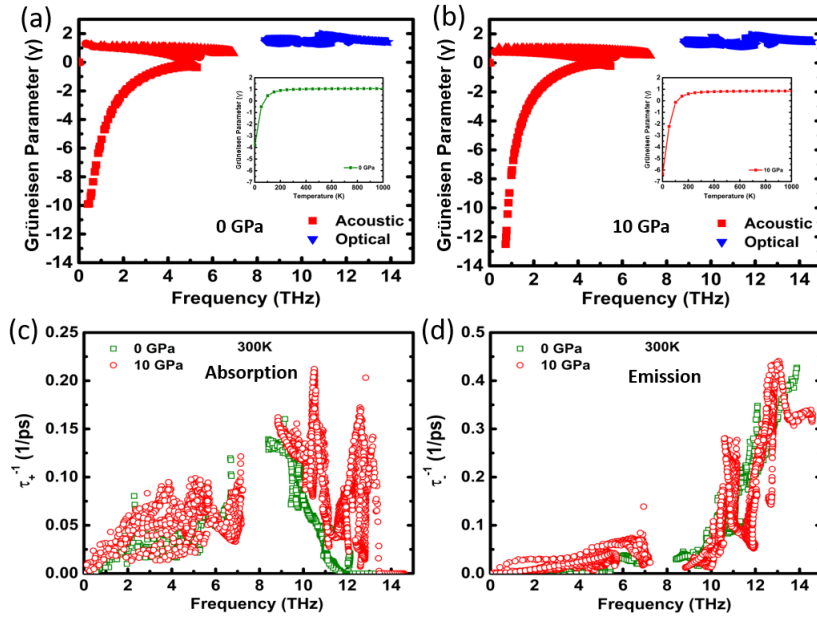


FIG. 7. Calculated mode Grüneisen parameters (γ) of ML-MoS₂ as a function of phonon frequency at (a) 0 GPa and (b) 10 GPa. The variation in the Grüneisen parameter with temperature at 0 and 10 GPa is shown in the insets of (a) and (b). The phonon scattering rates at 300 K under 0 and 10 GPa hydrostatic pressure corresponding to the (c) absorption and (d) emission processes.

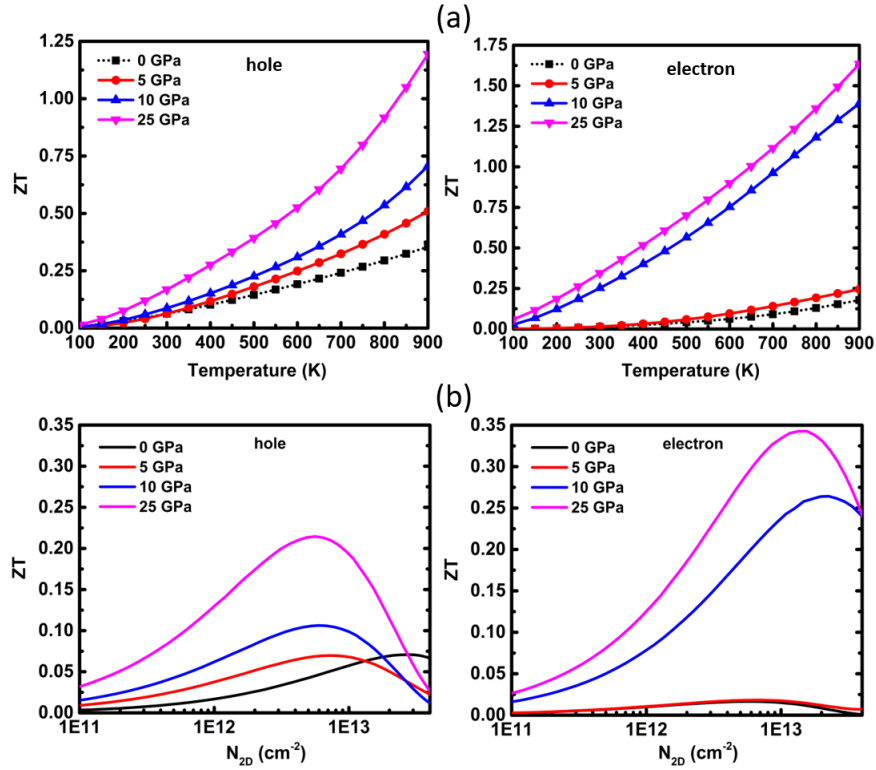


FIG. 8. Variation in the thermoelectric figure of merit (zT) of ML-MoS₂ under hole and electron doping at various hydrostatic pressure as a function of (a) temperature at a fixed carrier concentration of $1.3 \times 10^{13} / \text{cm}^2$ and (b) carrier concentration at a fixed temperature of 300 K.

restriction, the absorption process (+) is dominant in the low frequency regime, whereas the emission process (-) is

dominant in the high frequency regime. With increasing pressure, the scattering rates associated with both processes increase, mainly the absorption one (τ_+^{-1}), resulting in the decrease of the phonon relaxation time. The increase in the probability of phonon scattering is attributed to the shortening of the interatomic distances and the increased bond anharmonicity under the application of pressure.

Finally, combining all the calculated transport parameters, such as the S , $S^2\sigma$, τ , κ , the thermoelectric efficiency or the zT of ML-MoS₂ has been estimated and its variation with temperature (T) and carrier concentration (N_{2D}) has been explored under different pressure conditions (see Fig. 8). The room temperature zT values obtained with pristine ML-MoS₂ with a carrier concentration of $1.3 \times 10^{13} / \text{cm}^2$ are only 0.05 and 0.01 for hole and electron doping, respectively. Such a low value of zT is not useful for practical application purposes. With the application of pressure, the zT value under hole and electron doping is found to increase significantly. For holes the zT value is found to increase monotonically with pressure, whereas for electrons a dramatic enhancement is observed starting from 10 GPa. At a pressure of 25 GPa, the room temperature zT values of ML-MoS₂ are found to be 0.17 and 0.35 for hole and electron doping, which are significantly higher compared to the zero pressure values. Apart from the reduction in lattice thermal conductivity, the gradual increase in hole mobility and relaxation time with pressure act behind the enhancement of the zT value under hole doping. However, for electrons, the increase in thermopower (S) due to the valley convergence in the conduction band (CB) and the involvement of the CB- Λ in electronic transport with significantly high carrier mobility acts in unison to result in the remarkable increase in zT . In addition to the pressure induced enhancement, the zT values are found to increase significantly with increasing temperature, as can be seen in Fig. 8 (a). The highest zT values at 900 K obtained with hole and electron doping are 1.21 and 1.63, respectively. These zT values, obtained with ML-MoS₂ are comparable to any good commercial thermoelectric material. Also, it is worth noting that the enhanced thermoelectric performance is not only achieved at a specific doping concentration of $1.3 \times 10^{13} / \text{cm}^2$; instead, the enhancement can be achieved for a range of doping concentrations. To further support this point, the variation in the zT of ML-MoS₂ at 300 K as a function of doping concentration under different pressures is shown in Fig. 8 (b). It is evident that a much improved thermoelectric performance can be obtained at the optimal doping concentration when a certain amount of pressure is applied. Notably, the concurrent increase in zT for both electron and hole doping is highly beneficial for its integration in thermoelectric devices, where both the p- and n-legs are preferably made from a single material with high thermoelectric efficiency.

IV. CONCLUSIONS

In summary, first principles calculations have been performed to analyze the hydrostatic strain induced changes in the electronic structure and transport properties of ML-MoS₂. The application of external pressure in ML-MoS₂ induces a direct to indirect band gap transition at around 10 GPa due to the shifting of the CBM from K to Λ , which also increases the valley degeneracy with the band edge at the K point still lying close in energy to the CBM at Λ . Owing to this increase in valley degeneracy, the thermopower (S) and thereby, the power factor ($S^2\sigma$) show an increase for the electron doping. Also, the application of hydrostatic pressure results in an increase in electron mobility (μ) and a dramatically enhanced relaxation time (τ), which follows from the low deformation potential associated with CB- Λ . On the other hand, the lattice thermal conductivity (κ_L) is also found to decrease significantly with increasing pressure due to the increase in anharmonicity and the resulting phonon scattering. The pressure induced increase in S and μ , and the decrease in κ_L act in unison to result in a large increase in zT . At 900 K with an external pressure of 25 GPa, zT values of 1.21 and 1.63 are achieved for the hole and the electron doping, respectively, which are significantly higher compared to that for the zero pressure case. This study, therefore, highlights the importance of hydrostatic pressure in improving the thermoelectric properties of ML-MoS₂. Given that the application of hydrostatic pressure increase the efficiency for both the n-type and p-type doping, this fairly straight forward method can be beneficial for the designing of thermoelectric module, where both legs should be preferably made of the same material. Also, the proposed approach is expected to be equally useful for all other semiconducting TMDCs with similar crystal structures.

ACKNOWLEDGMENTS

The first-principles calculations have been performed using the supercomputing facility of IIT Kharagpur established under the National Supercomputing Mission (NSM), Government of India and supported by the Centre for Development of Advanced Computing (CDAC), Pune. AB acknowledges SERB POWER grant (SPG/2021/003874) and BRNS regular grant (BRNS/37098) for the financial assistance. SC acknowledges MHRD, India, for financial

support.

-
- [1] Owusu, P. A.; Asumadu-Sarkodie, S. A review of renewable energy sources, sustainability issues and climate change mitigation. *Cogent Engineering* **2016**, *3*, 1167990.
 - [2] Zhang, X.; Zhao, L.-D. Thermoelectric materials: Energy conversion between heat and electricity. *Journal of Materiomics* **2015**, *1*, 92–105.
 - [3] Freer, R.; Powell, A. V. Realising the potential of thermoelectric technology: A Roadmap. *Journal of Materials Chemistry C* **2020**, *8*, 441–463.
 - [4] Orr, B.; Akbarzadeh, A. Prospects of waste heat recovery and power generation using thermoelectric generators. *Energy Procedia* **2017**, *110*, 250–255.
 - [5] Bilec, D. I.; Hautier, G.; Waroquier, D.; Rignanese, G.-M.; Ghosez, P. Low-dimensional transport and large thermoelectric power factors in bulk semiconductors by band engineering of highly directional electronic states. *Physical review letters* **2015**, *114*, 136601.
 - [6] Pei, Y.; Shi, X.; LaLonde, A.; Wang, H.; Chen, L.; Snyder, G. J. Convergence of electronic bands for high performance bulk thermoelectrics. *Nature* **2011**, *473*, 66–69.
 - [7] Dresselhaus, M. S.; Chen, G.; Tang, M. Y.; Yang, R.; Lee, H.; Wang, D.; Ren, Z.; Fleurial, J.-P.; Gogna, P. New directions for low-dimensional thermoelectric materials. *Advanced materials* **2007**, *19*, 1043–1053.
 - [8] Zhang, P.; Gong, L.; Lou, Z.; Xu, J.; Cao, S.; Zhu, J.; Yan, H.; Gao, F. Reduced lattice thermal conductivity of perovskite-type high-entropy (Ca_{0.25}Sr_{0.25}Ba_{0.25}RE_{0.25})TiO₃ ceramics by phonon engineering for thermoelectric applications. *Journal of Alloys and Compounds* **2022**, *898*, 162858.
 - [9] Gautam, A. K.; Faraz, M.; Khare, N. Enhanced thermoelectric properties of MoS₂ with the incorporation of reduced graphene oxide (RGO). *Journal of Alloys and Compounds* **2020**, *838*, 155673.
 - [10] Li, H.-p.; Zhang, R.-q. Vacancy-defect-induced diminution of thermal conductivity in silicene. *Europhysics Letters* **2012**, *99*, 36001.
 - [11] Ding, Z.; Pei, Q.-X.; Jiang, J.-W.; Zhang, Y.-W. Manipulating the thermal conductivity of monolayer MoS₂ via lattice defect and strain engineering. *The Journal of Physical Chemistry C* **2015**, *119*, 16358–16365.
 - [12] Bera, J.; Sahu, S. Strain induced valley degeneracy: A route to the enhancement of thermoelectric properties of monolayer WS₂. *RSC advances* **2019**, *9*, 25216–25224.
 - [13] Jin, Z.; Liao, Q.; Fang, H.; Liu, Z.; Liu, W.; Ding, Z.; Luo, T.; Yang, N. A revisit to high thermoelectric performance of single-layer MoS₂. *Scientific reports* **2015**, *5*, 1–7.
 - [14] Jia, P.-Z.; Xie, Z.-X.; Deng, Y.-X.; Zhang, Y.; Tang, L.-M.; Zhou, W.-X.; Chen, K.-Q. High thermoelectric performance induced by strong anharmonic effects in monolayer (PbX)₂ (X = S, Se, Te). *Applied Physics Letters* **2022**, *121*, 043901.
 - [15] Nguyen, V. Q.; Kim, J.; Cho, S. A review of SnSe: Growth and thermoelectric properties. *Journal of the Korean Physical Society* **2018**, *72*, 841–857.
 - [16] Wang, Q. H.; Kalantar-Zadeh, K.; Kis, A.; Coleman, J. N.; Strano, M. S. Electronics and optoelectronics of two-dimensional transition metal dichalcogenides. *Nature nanotechnology* **2012**, *7*, 699–712.
 - [17] Guo, H.-H.; Yang, T.; Tao, P.; Zhang, Z.-D. Theoretical study of thermoelectric properties of MoS₂. *Chinese Physics B* **2013**, *23*, 017201.
 - [18] Akinwande, D.; Petrone, N.; Hone, J. Two-dimensional flexible nanoelectronics. *Nature communications* **2014**, *5*, 5678.
 - [19] Chaudhuri, S.; Das, A. K.; Das, G. P.; Dev, B. N. Strain induced effects on the electronic and phononic properties of 2H and 1T monolayer MoS₂. *Physica B: Condensed Matter* **2023**, *655*, 414701.
 - [20] Radisavljevic, B.; Radenovic, A.; Brivio, J.; Giacometti, V.; Kis, A. Single-layer MoS₂ transistors. *Nature nanotechnology* **2011**, *6*, 147–150.
 - [21] Patel, A.; Singh, D.; Sonvane, Y.; Thakor, P.; Ahuja, R. High thermoelectric performance in two-dimensional Janus monolayer material WS-X (X = Se and Te). *ACS applied materials & interfaces* **2020**, *12*, 46212–46219.
 - [22] Kumar, S.; Schwingenschlogl, U. Thermoelectric response of bulk and monolayer MoSe₂ and WSe₂. *Chemistry of Materials* **2015**, *27*, 1278–1284.
 - [23] Wang, H.; Lan, Y.-S.; Dai, B.; Zhang, X.-W.; Wang, Z.-G.; Ge, N.-N. Improved thermoelectric performance of monolayer HfS₂ by strain engineering. *ACS omega* **2021**, *6*, 29820–29829.
 - [24] Su, Y.; Ebrish, M. A.; Olson, E. J.; Koester, S. J. SnSe₂ field-effect transistors with high drive current. *Applied Physics Letters* **2013**, *103*, 263104.
 - [25] Bhattacharyya, S.; Pandey, T.; Singh, A. K. Effect of strain on electronic and thermoelectric properties of few layers to bulk MoS₂. *Nanotechnology* **2014**, *25*, 465701.
 - [26] Huang, W.; Luo, X.; Gan, C. K.; Quek, S. Y.; Liang, G. Theoretical study of thermoelectric properties of few-layer MoS₂ and WSe₂. *Physical Chemistry Chemical Physics* **2014**, *16*, 10866–10874.
 - [27] Wickramaratne, D.; Zahid, F.; Lake, R. K. Electronic and thermoelectric properties of few-layer transition metal dichalcogenides. *The Journal of chemical physics* **2014**, *140*, 124710.
 - [28] Jena, N.; De Sarkar, A., et al. Compressive strain induced enhancement in thermoelectric-power-factor in monolayer MoS₂ nanosheet. *Journal of Physics: Condensed Matter* **2017**, *29*, 225501.

- [29] Guo, H.; Yang, T.; Tao, P.; Wang, Y.; Zhang, Z. High pressure effect on structure, electronic structure, and thermoelectric properties of MoS₂. *Journal of Applied Physics* **2013**, *113*, 013709.
- [30] Xiang, J.; Ali, R. N.; Yang, Y.; Zheng, Z.; Xiang, B.; Cui, X. Monolayer MoS₂ thermoelectric properties engineering via strain effect. *Physica E: Low-dimensional Systems and Nanostructures* **2019**, *109*, 248–252.
- [31] Chaudhuri, S.; Bhattacharya, A.; Das, A. K.; Das, G. P.; Dev, B. N. Strain driven anomalous anisotropic enhancement in the thermoelectric performance of monolayer MoS₂. *Applied Surface Science* **2023**, *626*, 157139.
- [32] Hippalgaonkar, K.; Wang, Y.; Ye, Y.; Qiu, D. Y.; Zhu, H.; Wang, Y.; Moore, J.; Louie, S. G.; Zhang, X. High thermoelectric power factor in two-dimensional crystals of MoS₂. *Physical Review B* **2017**, *95*, 115407.
- [33] Kayyalha, M.; Maassen, J.; Lundstrom, M.; Shi, L.; Chen, Y. P. Gate-tunable and thickness-dependent electronic and thermoelectric transport in few-layer MoS₂. *Journal of Applied Physics* **2016**, *120*, 134305.
- [34] Buscema, M.; Barkelid, M.; Zwiller, V.; van der Zant, H. S.; Steele, G. A.; Castellanos-Gomez, A. Large and tunable photothermoelectric effect in single-layer MoS₂. *Nano letters* **2013**, *13*, 358–363.
- [35] Rai, D.; Vu, T. V.; Laref, A.; Hossain, M. A.; Haque, E.; Ahmad, S.; Khenata, R.; Thapa, R. Electronic properties and low lattice thermal conductivity (κ) of mono-layer (ML) MoS₂: FP-LAPW incorporated with spin-orbit coupling (SOC). *Rsc Advances* **2020**, *10*, 18830–18840.
- [36] Yan, R.; Simpson, J. R.; Bertolazzi, S.; Brivio, J.; Watson, M.; Wu, X.; Kis, A.; Luo, T.; Hight Walker, A. R.; Xing, H. G. Thermal conductivity of monolayer molybdenum disulfide obtained from temperature-dependent Raman spectroscopy. *ACS nano* **2014**, *8*, 986–993.
- [37] Guo, S.-D.; Li, Y.-F.; Guo, X.-S. Predicted Janus monolayer ZrSSe with enhanced n-type thermoelectric properties compared with monolayer ZrS₂. *Computational Materials Science* **2019**, *161*, 16–23.
- [38] Kong, S.; Wu, T.; Zhuang, W.; Jiang, P.; Bao, X. Realizing p-type MoS₂ with enhanced thermoelectric performance by embedding VMO₂S₄ nano-inclusions. *The Journal of Physical Chemistry B* **2018**, *122*, 713–720.
- [39] Gangwar, P.; Kumar, S.; Khare, N. Ultrahigh thermoelectric performance of 2H-MoS₂ nanosheets with incorporated conducting secondary phase. *Materials Research Express* **2019**, *6*, 105062.
- [40] Lv, H.; Lu, W.; Shao, D.; Lu, H.; Sun, Y. Strain-induced enhancement in the thermoelectric performance of a ZrS₂ monolayer. *Journal of Materials Chemistry C* **2016**, *4*, 4538–4545.
- [41] Chaudhuri, S.; Das, A. K.; Das, G. P.; Dev, B. N. Ab Initio Study of Electronic and Lattice Dynamical Properties of Monolayer ZnO Under Strain. *Journal of Electronic Materials* **2023**, *52*, 1633–1643.
- [42] Pu, J.; Zhang, Y.; Wada, Y.; Tse-Wei Wang, J.; Li, L.-J.; Iwasa, Y.; Takenobu, T. Fabrication of stretchable MoS₂ thin-film transistors using elastic ion-gel gate dielectrics. *Applied Physics Letters* **2013**, *103*, 023505.
- [43] Castellanos-Gomez, A.; Roldán, R.; Cappelluti, E.; Buscema, M.; Guinea, F.; van der Zant, H. S.; Steele, G. A. Local strain engineering in atomically thin MoS₂. *Nano letters* **2013**, *13*, 5361–5366.
- [44] Bertolazzi, S.; Brivio, J.; Kis, A. Stretching and breaking of ultrathin MoS₂. *ACS nano* **2011**, *5*, 9703–9709.
- [45] Jiang, J. W. The buckling of single-layer MoS₂ under uniaxial compression. *Nanotechnology* **2014**, *25*, 355402.
- [46] Li, Y.; Chen, P.; Zhang, C.; Peng, J.; Gao, F.; Liu, H. Molecular dynamics simulation on the buckling of single-layer MoS₂ sheet with defects under uniaxial compression. *Computational Materials Science* **2019**, *162*, 116–123.
- [47] Peelaers, H.; Van de Walle, C. Elastic constants and pressure-induced effects in MoS₂. *The Journal of Physical Chemistry C* **2014**, *118*, 12073–12076.
- [48] Fu, L.; Wan, Y.; Tang, N.; Ding, Y.-m.; Gao, J.; Yu, J.; Guan, H.; Zhang, K.; Wang, W.; Zhang, C., et al. K-A crossover transition in the conduction band of monolayer MoS₂ under hydrostatic pressure. *Science advances* **2017**, *3*, e1700162.
- [49] Chi, Z.-H.; Zhao, X.-M.; Zhang, H.; Goncharov, A. F.; Lobanov, S. S.; Kagayama, T.; Sakata, M.; Chen, X.-J. Pressure-induced metallization of molybdenum disulfide. *Physical review letters* **2014**, *113*, 036802.
- [50] Kresse, G.; Furthmüller, J. Efficient iterative schemes for ab initio total-energy calculations using a plane-wave basis set. *Physical review B* **1996**, *54*, 11169.
- [51] Kresse, G.; Furthmüller, J. Efficiency of ab-initio total energy calculations for metals and semiconductors using a plane-wave basis set. *Computational materials science* **1996**, *6*, 15–50.
- [52] Kresse, G.; Joubert, D. From ultrasoft pseudopotentials to the projector augmented-wave method. *Physical review b* **1999**, *59*, 1758.
- [53] Perdew, J. P.; Burke, K.; Ernzerhof, M. Generalized gradient approximation made simple. *Physical review letters* **1996**, *77*, 3865.
- [54] Monkhorst, H. J.; Pack, J. D. Special points for Brillouin-zone integrations. *Physical review B* **1976**, *13*, 5188.
- [55] Fan, X.; Chang, C.-H.; Zheng, W.; Kuo, J.-L.; Singh, D. J. The electronic properties of single-layer and multilayer MoS₂ under high pressure. *The Journal of Physical Chemistry C* **2015**, *119*, 10189–10196.
- [56] Madsen, G. K.; Singh, D. J. BoltzTraP. A code for calculating band-structure dependent quantities. *Computer Physics Communications* **2006**, *175*, 67–71.
- [57] Bardeen, J.; Shockley, W. Deformation potentials and mobilities in non-polar crystals. *Physical review* **1950**, *80*, 72.
- [58] Togo, A.; Tanaka, I. First principles phonon calculations in materials science. *Scripta Materialia* **2015**, *108*, 1–5.
- [59] Togo, A.; Chaput, L.; Tanaka, I. Distributions of phonon lifetimes in Brillouin zones. *Physical review B* **2015**, *91*, 094306.
- [60] Das, R.; Rakshit, B.; Debnath, S.; Mahadevan, P. Microscopic model for the strain-driven direct to indirect band-gap transition in monolayer MoS₂ and ZnO. *Physical Review B* **2014**, *89*, 115201.
- [61] Goldsmid, H.; Sharp, J. Estimation of the thermal band gap of a semiconductor from Seebeck measurements. *Journal of electronic materials* **1999**, *28*, 869–872.
- [62] Wiktor, J.; Pasquarello, A. Absolute deformation potentials of two-dimensional materials. *Physical Review B* **2016**, *94*, 245411.

- [63] Hung, N. T.; Nugraha, A. R.; Saito, R. Two-dimensional MoS₂ electromechanical actuators. *Journal of Physics D: Applied Physics* **2018**, *51*, 075306.
- [64] Rawat, A.; Jena, N.; De Sarkar, A., et al. A comprehensive study on carrier mobility and artificial photosynthetic properties in group VI B transition metal dichalcogenide monolayers. *Journal of Materials Chemistry A* **2018**, *6*, 8693–8704.
- [65] Cai, Y.; Lan, J.; Zhang, G.; Zhang, Y.-W. Lattice vibrational modes and phonon thermal conductivity of monolayer MoS₂. *Physical Review B* **2014**, *89*, 035438.